

# RaliSense: Extending WiFi Respiratory Detection Range by Rapid Alignment of Dynamic Components

Linqing Gui, Siyi Zheng, Zhengxin Guo, Zhetao Li, Ming Gao, Schahram Dustdar, Fu Xiao

**Abstract**—WiFi based respiratory detection has attracted increasing attentions due to its ubiquity and convenience. In Non-Line-of-Sight (NLoS) scenarios, WiFi signals reflected from human target are blocked by obstacles and become much weaker, thus limiting the sensing range and hindering the practical deployment. The existing best respiratory detection system extended the sensing range by scaling and aligning dynamic components in WiFi signals. However, its dynamic component scaling causes the amplification of noise, while its dynamic component alignment increases computation complexity due to the traversal on all possible rotation angles. To address the above issues, in this paper we first build WiFi sensing range models for respiratory detection in NLoS scenario, find factors that limit the sensing range, and then propose a new respiratory detection system named RaliSense which can further rapidly extend the sensing range in NLoS scenario. The main idea of RaliSense is rapidly aligning dynamic components without amplifying noise, based on change direction vector and CSI ratio sum polarity of dynamic components. The proposed change direction vector is obtained by calculating the direction on which the noisy dynamic components have the maximum variance, and CSI ratio sum polarity is then obtained by summing the dynamic components which have been rotated by the change direction vector. According to the CSI ratio sum polarity, the rotation angle is quickly adjusted for aligning dynamic components. Extensive simulation and experiment results verify the effectiveness of our proposed sensing range models. The results also demonstrate that our proposed system RaliSense can effectively extend sensing range in NLoS scenario, achieving a 22.7% improvement over the best existing work but spending only a quarter of its computation time.

**Index Terms**—Wireless Sensing, Sensing Range, Channel State Information (CSI)

## I. INTRODUCTION

**I**N recent years, with the rapid development of wireless technology, widely deployed commodity WiFi devices have been utilized for achieving ubiquitously contactless sensing. A

large variety of applications based on WiFi sensing have been developed, such as fine-grained respiration detection [1], [2], [3], [4], [5], activity recognition [6], [7], [8], indoor positioning [9], [10], fall detection [11], [12], and size measurement [13]. In comparison to traditional sensing platforms such as cameras or wearable devices, WiFi sensing has advantages of device-free convenience, low cost and privacy protection. Therefore, the contactless WiFi-based solution has been recently a more desirable choice.

Channel state information (CSI) provides fine-grained subcarrier-level physical layer information of WiFi [14], [15]. Reflected by the chest, WiFi signals change with the respiration of nearby person, resulting in the change of CSI. By capturing CSI characteristics, respiratory rate and respiration waveform can be estimated. In NLoS scenarios, since obstacles block the direct signal between human and WiFi device, WiFi signals reflected by human target become much weaker, affecting accurate detection of respiration rate and also limiting the sensing range [16]. The restricted sensing range greatly reduces its practicability. Due to short sensing range, more WiFi devices need to be deployed in the same sensing area to avoid the existence of blind sectors. This will increase the overall cost and hinder widespread application.

The modeling and extending of WiFi sensing range have been studied these years. A Fresnel diffraction model was proposed in [17] to quantify the relationship between human position and respiratory detectability. This model can guide users to find good positions for respiratory detection, but can only be used to build a basic sensing range model in LoS scenario. The characteristics of Fresnel reflection model was further summarized in [18] for deriving a sensing limit of WiFi signal, but the interval of sensing limit was derived rather than a precise sensing limit because Fresnel zones differ from fine-grained channel state information. Wiphone [19] modeled the relationship between CSI signal reflected from the environment and a target's chest displacement in a NLoS scenario. However, this model is only applicable for CSI-amplitude-based respiratory detection, and CSI amplitude is not as precise as CSI phase [20]. FarSense [21] proposed a CSI-ratio model to extend the sensing range of respiratory detection. Although it can remove phase offset and reduce amplitude noise based on the CSI ratio, only one pair of antennas and one subcarrier with the maximum breathing-to-noise ratio are used, limiting its capacity of sensing range extension. EMA [22] exploited spatial diversity to extend sensing range of respiratory detection. CSI data of all the

This work is supported in part by the National Science Fund for Distinguished Young Scholars (Grant 62125203), the National Natural Science Foundation of China (Grant 62372246), the National Key Research and Development Program of China (Grant 2023YFB3107500).

L. Gui, S. Zheng, Z. Guo, M. Gao and F. Xiao are with the School of Computer Science, Nanjing University of Posts and Telecommunications, Nanjing 210023, China (E-mail: guilq@njupt.edu.cn, 1022040920@njupt.edu.cn, guozhengxin\_gzx@163.com, gaomingppm@gmail.com, xiaof@njupt.edu.cn). (Corresponding author: Fu Xiao.)

Z. Li is with the College of Information Science and Technology, Jinan University, Guangzhou, 510632, China (E-mail: liztchina@hotmail.com).

S. Dustdar is with the Research Division of Distributed Systems, TU Wien, 1040 Vienna, Austria. He is also ICREA Research Professor, UPF, Barcelona, Spain (E-mail: dustdar@gmail.com).

antenna pairs were combined in a weighted way to enhance sensing-signal-to-noise ratio. Though the spatial diversity has been fully exploited, EMA lacks the integration of frequency diversity and time diversity.

DiverSense [23] enhanced the quality of the sensing signal by further leveraging the frequency and time diversity of WiFi signal. Although DiverSense is the best existing respiratory detection system, two problems still need to be addressed. The first problem is that the scaling of dynamic components causes the amplification of noise. To maximize the sensing range, DiverSense scales and aligns the dynamic components in all subcarriers. During the scaling, a dynamic component is amplified as well as the additional noise. The second problem is that the alignment of dynamic components increases computation complexity. Since the phases of CSI dynamic components are always different, rotating the CSI ratio signals is essential to align the dynamic components. Two dynamic components are aligned by continuously rotating one of them until their distance is minimized, requiring the traversal of every possible angle. The traversal method results in high computation complexity.

In order to solve the aforementioned two problems, we first build WiFi sensing range models for respiratory detection in NLoS scenario, find factors that limit the sensing range, and then propose a new respiratory detection system named RaliSense which can further rapidly extend the sensing range in NLoS scenario. Three challenges need to be tackled before our idea can be applied to extend the sensing range:

- Modeling the sensing range of respiratory detection is challenging due to two factors. First, the sensing range is closely related to the adopted respiratory detection system, but the state-of-art respiratory detection systems are complex. Second, in NLoS scenarios, signal propagation environment is more complex.
- Extending the sensing range of respiratory detection in NLoS scenarios is challenging, since WiFi signals reflected from human target are blocked by obstacles and become much weaker. To enhance the sensing quality, dynamic components of CSI ratio need to be aligned. As one important step in traditional dynamic component alignment, the scaling standardizes the sizes of dynamic components, but also amplifies noise. We need to achieve dynamic component alignment without amplifying noise.
- Effectively reducing the computation complexity of the existing most advanced respiratory detection system is challenging. In the existing best system, dynamic component alignment requires traversing all possible angles and calculating the sum of sample difference at each angle. This traversal method results in excessive algorithmic overhead. We need to quickly align the dynamic components without traversing all rotation angles.

To tackle the above challenges, we have conducted a series of work. First, we define the sensing range of respiratory detection by formulating it as a mathematical problem, derive dynamic propagation path distance in NLoS scenario, and further derive sensing range models for respiratory detection systems. Second, we propose a more precise CSI ratio model

and a new respiratory detection system which can align dynamic components without amplifying noise. It is fulfilled by our proposed change direction vector of dynamic components and the polarity of CSI ratio sum. The change direction vector represents the phase change direction of dynamic component, while the polarity of CSI ratio sum can solve the rotation angle ambiguity problem. Third, our proposed respiratory detection system allows us to quickly determine the rotation angle without traversing all possible angles. The quickly derived rotation angle is used to fulfill rapid alignment of dynamic components. As a result, the computation complexity can be effectively reduced.

The main contributions of this work can be summarized as follows.

- We derive sensing range models for different respiratory detection systems in NLoS scenario. This work provides a theoretical foundation for research on sensing range of various fine-grained sensing tasks as well as their system design.
- We propose RaliSense, a new respiratory detection system that can quickly extend the sensing range in NLoS scenario. One important feature of RaliSense is the rapid alignment of dynamic components without amplifying noise. The change direction vector is quickly found by calculating the direction on which the noisy dynamic components have the maximum variance. The rotation angle for aligning dynamic components is then quickly determined by both the change direction vector and the CSI ratio sum polarity. The latter can quickly solve the the rotation angle ambiguity problem.
- We build a prototype of RaliSense and evaluate its performance by extensive simulations and experiments. The results verify the effectiveness of our proposed sensing range models. Moreover, the results demonstrate that our proposed system RaliSense can effectively extend sensing range in NLoS scenario, achieving a 22.7% improvement over the best existing work but only spending a quarter of its computation time.

The rest of this paper is organized as follow. Section II introduces the most related work. Section III presents basic CSI model in NLoS scenario and existing advanced respiratory detection systems. The definition of WiFi-based sensing range and the derivation of sensing range models are illustrated in Section IV, while Section V presents a more precise CSI ratio model and our new respiratory detection system. Then Section VI presents the simulation and experiment results together with the analysis. Finally, Section VII gives the conclusion.

## II. RELATED WORK

### A. WiFi-based Contact-free Respiratory Sensing

WiFi-based contact-free respiratory sensing systems become attractive because they meet both non-intrusive and cost-effective requirements. Recent WiFi-based respiratory sensing methods mainly used the amplitude and phase information of CSI for sensing. BreathTrack [24] exploited the phase variation of CSI to track human breath. FullBreathe [25] eliminated

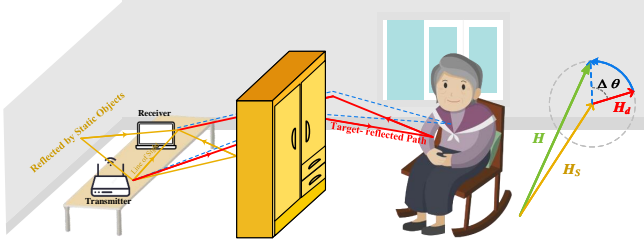


Fig. 1. Example of human sensing with WiFi CSI in NLoS scenario.

blind spots of respiratory sensing by conjugate multiplication of CSI amplitude and phase between antennas. Based on Fresnel theory, the approach proposed in [26] used multiple transceiver devices to estimate the respiratory rate. MultiSense [27] exploited blind source signal separation and independent component analysis to simultaneously extract multi-person respiratory patterns. The work in [28] proposed a Matching Pursuit based Joint Angle and Respiration Estimation algorithm, enabling the reliable separation of the respiration of multiple targets. PresSense [29] proposed the Peak Distance Histogram feature to achieve more accurate respiratory detection. WiResP [30] treated the spectrum of CSI data as an image and proposed an image-based continuity checker module to reliably capture respiration. However, image processing results in significant computational overhead, making it challenging to meet real-time requirements. ResFi [31] and the work in [32] detected respiration by proposing learning-based methods, but they require further training in new environments, which limits their applicability.

### B. WiFi-Based Contact-Free Sensing Range

WiFi-based contact-free sensing range has been studied these years. Zhang et al. [17] developed a mathematical model to relate one's location to the detectability of respiratory within the First Fresnel Zone (FFZ). FarSense [21] proposed a CSI-ratio model to address the respiratory blind spots problem and increased the sensing range. It required the synchronization of CSI stream clocks of two receiving antennas. WiBorder [33] extracted a new metric DCM-CSI from the CSI conjugate multiplication between two antennas. Based on this metric, a stable threshold line was found to distinguish direct and indirect signals, then the walls in the environment were used to determine sensing range. One main constraint of this system was its coarse-grained perception of humans. Zhang et al. [18] further summarized the characteristics of Fresnel reflection model for human RF sensing and derived a sensing limit of WiFi signal. However, the precise sensing range was still unknown, because Fresnel zones were a series of concentric ellipsoids of alternating strength and still differs from fine-grained channel state information. EMA [22] exploited spatial diversity to extend sensing range of respiratory detection. CSI data of all the antenna pairs are combined to enhance sensing-signal-to-noise ratio. DiverSense [23] enhanced the sensing quality by leveraging the frequency and time diversity of WiFi signal. The CSI samples are aggregated to obtain dynamic

components, which are aligned and combined across all sub-carriers. Although DiverSense is the best existing respiratory detection system, its dynamic component scaling causes noise amplification and its dynamic component alignment increases computation complexity.

## III. PRELIMINARY

In this section, we first describe how respiration influences wireless channels between WiFi transmitter and receiver, providing basic CSI model for sensing respiration. Built on the basic CSI model, existing respiratory detection methods further processed CSI data in different ways. So, we then introduce how CSI data were processed by the existing advanced methods such as EMA and DiverSense.

### A. Basic CSI Model

In the concerned NLoS scenario, obstacles such as cabinet and screen block the direct signal between human and sensing device. The signal arriving at the receiver is actually a superposition of signals coming from multiple paths. These paths can be grouped into static paths and dynamic paths. Each static path does not vary with time, while each dynamic path varies with target movement. The CSI in NLoS scenarios can be denoted as:

$$H(f, t) = \sum_{i \in L_S} H_i(f, t) + \sum_{j \in L_{D, NLoS}} H_j(f, t), \quad (1)$$

where  $L_S$  denotes static paths,  $L_{D, NLoS}$  denotes dynamic NLoS paths,  $f$  is the carrier frequency,  $H_i(f, t)$  is the  $i$ -th static path CSI, and  $H_j(f, t)$  is the  $j$ -th dynamic path CSI.

Fig. 1 shows CSI-based respiratory detection in a typical NLoS scenario. The dynamic path signals are reflected from the target. The slight displacement of the target causes a phase change. The static path signal comprises signals reflected from stationary objects in the surroundings (such as walls and closet) and the direct path signal, forming a constant complex number. We further take noise into consideration and the CSI can then be denoted as:

$$H(f, t) = S(f) + \sum_{i \in L_{d, NLoS}} \alpha_i(f, t) e^{-j2\pi f \frac{d_i(t)}{c}} + \epsilon(f, t), \quad (2)$$

where  $S(f)$  is the static component,  $H_{d, NLoS}(f, t)$  represents the dynamic component,  $c$  is the speed of light,  $\alpha_i(f, t)$  represents the amplitude attenuation and initial phase of  $i$ -th dynamic path,  $d_i(t)$  is the distance of  $i$ -th dynamic path, and  $\epsilon(f, t)$  is the noise, which is assumed as an additive white Gaussian noise.

### B. Respiratory Detection Using EMA

In commodity WiFi devices, we can obtain multiple CSI data streams from different antenna pairs by MIMO (Multiple Input Multiple Output) techniques. To fully leverage these CSI data from all the antennas, EMA [22] combines them by a weighted sum, thereby enhancing sensing effect.

CSI data from different antenna pairs is rewritten as:

$$H_i(f, t) = S_i(f) + A_i(f, t) e^{-j2\pi f \frac{d_i(t)}{c}} + \epsilon_i(f, t) \quad (3)$$

where  $A_i(f, t) = \alpha_i(f, t)e^{-j2\pi f \frac{d_i(t) - d_1(t)}{c}}$ ,  $d_i(t) - d_1(t)$  denotes the length difference of the target-reflected path between the  $i$ -th antenna pair and the first antenna pair. Then, EMA combines all CSI data through weighting:

$$\bar{H}(t) = \sum_{i=1}^M w_i H_i(f, t), \quad (4)$$

In order to quantify the relation between noise and dynamic vector, EMA proposes a metric named sensing signal to-noise ratio (SSNR). It has been proven that a higher SSNR value corresponds to better sensing performance. By deriving the maximum SSNR, EMA obtains the optimal normalized weighting, which can be expressed as:

$$w_i = e^{j\theta_{ref}} \frac{A_i^*(f, t)}{\sqrt{\sum_{i=1}^M |A_i(f, t)|^2}}. \quad (5)$$

where  $A_i(f, t)$  is aligned to the same phase  $\theta_{ref}$ .

### C. Respiratory Detection Using DiverSense

DiverSense derives a CSI ratio model, and then proposes a signal alignment algorithm to align the phase of the multiple received sensing signals. The CSI ratio model is the basis of the algorithm, which can be expressed as:

$$\frac{H_p(f_i, t)}{H_q(f_i, t)} = \frac{\alpha_p(f_i, t)e^{-j2\pi f_i \frac{d_p(t)}{c}}}{S_q(f_i)} + \frac{S_p(f_i)}{S_q(f_i)} + \frac{\epsilon(f_i, t)}{S_q(f_i)}, \quad (6)$$

where  $H_p(f_i, t)$  and  $H_q(f_i, t)$  represent the CSI from any two different antenna pairs.

DiverSense finds that if two dynamic components have the same size, the two dynamic components can be aligned by rotating one of the signals until the distance of the corresponding samples is minimized. In this regard, DiverSense proposes a signal alignment algorithm. The algorithm has the following steps.

(1) Translation. The static component is removed by subtracting the average of enough CSI ratio samples:

$$\frac{H_p(f_i, t)}{H_q(f_i, t)} - E_{f_i} = \frac{|\alpha_p(f_i)| e^{-j\theta_{f_i}} (e^{-j\frac{2\pi f_i \Delta d(t)}{c}} - K) + \epsilon(f_i, t)}{S_q(f_i)}, \quad (7)$$

where  $E(f_i)$  is the average of CSI ratio samples,  $K = \frac{1}{T} \sum_{i=1}^T e^{-j2\pi f_i \frac{\Delta d(t)}{c}}$  is a complex value,  $T$  is the number of CSI ratio samples,  $\Delta d(t)$  is the distance change of dynamic path,  $\theta_{f_i}$  is the sum of  $\alpha_p(f_i)$ 's phase and  $2\pi f_i \frac{d_p(t) - \Delta d(t)}{c}$ .

(2) Scaling. Scale factor is obtained by calculating the moving average of the CSI ratio with a window size  $T'$  smaller than  $T$ :

$$Scale(f_i, t) = \frac{|\alpha_p(f_i, t)| |K'(f_i, t) - K|}{|S_q(f_i)|}. \quad (8)$$

$\frac{H_p(f_i, t)}{H_q(f_i, t)} - E(f_i, t)$  is scaled by  $\frac{|\alpha_p(f_i)| K_{dif}}{|S_q(f_i)|}$ , where the max value  $K'(f_i, t) - K$  is marked as  $K_{dif}$ . The scaled CSI ratios have dynamic components with same amplitude, which can be expressed as:

$$R_{p,q}(f_i, t) = \frac{e^{-j\theta_{f_i}} (e^{-j2\pi f_i \frac{\Delta d(t)}{c}} - K) + \frac{\epsilon(f_i, t)}{|\alpha_p(f_i)|}}{K_{dif}}, \quad (9)$$

(3) Rotation. DiverSense selects one CSI ratio as the reference and align other CSI ratios by calculating the minimum value of the sum of the distances between the corresponding samples. The final combined CSI can be expressed as:

$$\bar{H}(t) = \frac{\sum_{i=1}^{N_f} \left( e^{-j\theta_{f_1}} \left( e^{-j2\pi f_i \frac{\Delta d(t)}{c}} - K \right) + \epsilon'(f_i, t) \right)}{N_f K_{dif}}, \quad (10)$$

where  $N_f$  is the number of subcarriers, and  $\epsilon'(f_i, t)$  is the rotated noise.

## IV. MODEL THE SENSING RANGE OF RESPIRATORY DETECTION IN NLOS SCENARIOS

In this section, we model the sensing range of WiFi-based respiratory detection in NLoS scenario. First, we define the sensing range of WiFi-based respiratory detection by formulating it as a mathematical problem. Then, we model sensing range, beginning with the derivation of dynamic propagation path distance in NLoS scenario. At last, we derive the sensing range model of two advanced respiratory detection systems.

### A. Define WiFi-based Sensing Range

The sensing range of WiFi-based respiratory detection is defined as the longest distance between target and sensing device on the condition of respiratory rate detectability. We then explain three key components in the definition, i.e., the distance between target and sensing device, any concerned respiratory detection method and the respiratory rate detectability.

First, the distance between target person and sensing device, denoted as  $d_{PS}$ , is defined as the shorter of the distance from target to the receiver and the distance from target to the transmitter. If the longer distance is chosen as the distance between target and sensing device, it could lead to an exaggerated sensing range. Therefore, the shorter distance is used to define  $d_{PS}$ , which can be expressed as:

$$d_{PS} = \frac{d_{TP} + d_{PR} - |d_{TP} - d_{PR}|}{2}, \quad (11)$$

where  $d_{TP}$  is the distance between the target and the transmitter,  $d_{PR}$  is the distance between the target and the receiver.

The second component is the adopted respiratory detection method for estimating respiration rate. During the modelization of sensing range, the principle of the adopted respiratory detection method is formulated into CSI model, then the estimated respiration rate can be derived. More specifically, we modify the CSI model according to the data processing procedure of the specific respiratory detection method, thus obtain a processed CSI model. In the frequency domain of processed CSI model, the frequency which has the largest amplitude is regarded as the estimated respiration rate.

Third, respiratory rate detectability means that the respiratory rate can be accurately detected, i.e., the error between the estimated respiratory rate and the real respiratory rate should be small enough (e.g. smaller than a required threshold). The above error mainly comes from the imperfection of the adopted respiratory detection method. For example, it is hard to completely eliminate the noise in CSI data.

According to the above analysis on the three key components, the definition of sensing range can be expressed as an optimization problem:

$$d_{max} = \max d_{PS} \quad \text{s.t.} \quad \left| \widehat{f_{BR}}(d_{PS}) - f_{BR} \right| \leq \varepsilon_{BR}, \quad (12)$$

where  $\widehat{f_{BR}}(d_{PS})$  is the estimated respiratory rate,  $f_{BR}$  is the real respiratory rate, and  $\varepsilon_{BR}$  is the error threshold.

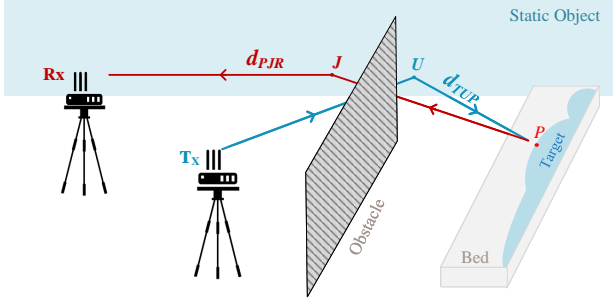


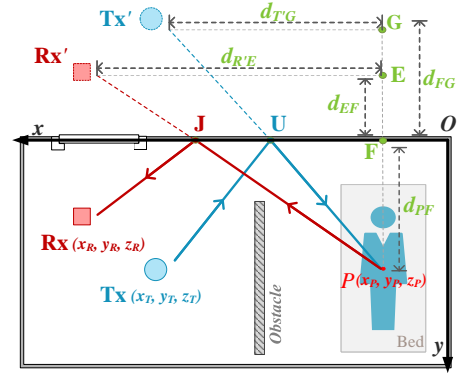
Fig. 2. Reflection path via the target.

### B. Derive the Dynamic Propagation Distance in NLoS Scenario

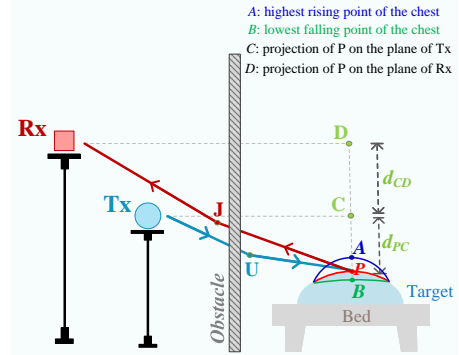
Before modeling the sensing range of the advanced methods, we need to derive dynamic propagation distance, which is an essential and common element in respiratory sensing model. More specifically, the relation between dynamic propagation distance and respiratory rate is derived. For the convenience of derivation, we remove the reflection paths via non-person reflectors, but retain the reflection path via the target. As shown in Fig. 2, the transmitter and receiver are denoted as  $Tx$  and  $Rx$ , respectively, the target's chest is denoted as  $P$ , and the two reflection points of the static object (i.e., the wall) are denoted as  $U$  and  $J$ , respectively. The positions of  $Tx$ ,  $Rx$  and the target  $P$  are denoted as  $(x_T, y_T, z_T)$ ,  $(x_R, y_R, z_R)$ ,  $(x_P, y_P, z_P)$ , respectively.

The dynamic propagation path is the reflection path  $Tx-U-P-J-Rx$ . The distance of the reflection path is denoted as  $d_i(f_{BR}, t)$ . Since multiple receiving antennas are used in this paper, we have  $d_i(f_{BR}, t) = d_{TUP}(f_{BR}, t) + d_{PJRx}(f_{BR}, t)$ .

Since WiFi signal dramatically attenuates with the prolongation of propagation path, we focus on the strongest dynamic path which is also the shortest dynamic path to achieve the best respiratory detection performance. So the multipath of the respiratory signal is simplified to the shortest NLoS path. As shown in Fig. 3, based on mirror symmetry, the path  $Tx-U-P-J-Rx$  is the shortest NLoS path. Fig. 3 (a) shows the top view of dynamic propagation path. The distances from the chest, transmitter, receiver to the wall are denoted as  $d_{PF}$ ,  $d_{FG}$ , and  $d_{FE}$ , respectively. The projections of the transmitter and the receiver on the wall are denoted as  $Tx'$  and  $Rx'$ , respectively. The distances from the transmitter and receiver to the centerline of the target are denoted as  $d_{T'G}$  and  $d_{R'E}$ , respectively. Fig. 3 (b) is the front view of dynamic propagation path.  $C$  and  $D$  denote the projection points of  $P$  on the planes of the transmitter and the receiver, respectively.



(a) Top view of dynamic propagation path



(b) Front view of dynamic propagation path

Fig. 3. Dynamic propagation path in NLoS scenario.

The distance  $d_{PC}(f_{BR}, t)$  and  $d_{PD}(f_{BR}, t)$  can denote  $P$ 's height relative to the transmitter and the receiver, respectively.

According to the top and front view of the dynamic propagation path, we have  $d_{TUP}(f_{BR}, t) = \sqrt{d_{T'P}^2 + d_{PC}^2(f_{BR}, t)}$ , where  $d_{T'P}$  can be expressed as:

$$d_{T'P} = \left( (d_{PF} + d_{FG})^2 + d_{T'G}^2 \right)^{\frac{1}{2}}. \quad (13)$$

As the chest of the target rises and falls with respiratory,  $P$  can rise to the highest point  $A$  and fall to the lowest point  $B$ . The range of  $d_{PC}(f_{BR}, t)$ 's change equals  $d_{AB}$ . The change of  $d_{PC}(f_{BR}, t)$  with respiratory is normally rhythmic and in the same frequency with the respiratory rate. Thus  $d_{PC}(f_{BR}, t)$  can be expressed as:

$$d_{PC}(f_{BR}, t) = \frac{1}{2} d_{AB} \sin 2\pi f_{BR} t + d_{BC} - \frac{1}{2} d_{AB}. \quad (14)$$

We substitute Eq. (13) and Eq. (14) into  $\sqrt{d_{T'P}^2 + d_{PC}^2(f_{BR}, t)}$  to obtain the relationship between  $d_{TUP}(f_{BR}, t)$  and respiration rate:

$$d_{TUP}(f_{BR}, t) = d_{T'P} \sqrt{1 + \left( \frac{d_{AB} \sin 2\pi f_{BR} t + 2d_{BC} - d_{AB}}{2d_{T'P}} \right)^2}. \quad (15)$$

Since  $d_{T'P}$  is much larger than  $d_{AB}$  and  $d_{BC}$ , we use Taylor expansion to expand the above equation and retain the first two terms. Then Eq. (15) is transformed to:

$$d_{TUP}(f_{BR}, t) = \frac{(2d_{BC} - d_{AB})d_{AB}}{4d_{T'P}} \sin 2\pi f_{BR} t + d_{T'P}. \quad (16)$$

Similarly,  $d_{PJR_i}(f_{BR}, t)$  is transformed to  $d_{PJR_i}(f_{BR}, t) = \frac{(2d_{BD}-d_{AB})d_{AB}}{4d_{PR'_i}} \sin 2\pi f_{BR}t + d_{PR'_i}$ . We have calculated the distances from the transmitter and receiver to the target. Thus, the distance of dynamic propagation path can be expressed as:

$$d_i(f_{BR}, t) = u_{Bi}d_{AB}\sin 2\pi f_{BR}t + d_{T'P} + d_{PR'_i}, \quad (17)$$

where

$$u_{Bi} = \frac{2d_{BC} - d_{AB}}{4d_{T'P}} + \frac{2d_{BD} - d_{AB}}{4d_{PR'_i}}, \quad (18)$$

$$d_{T'P} = \sqrt{(x_T - x_P)^2 + (y_T + y_P)^2 + (z_T - z_P)^2}, \quad (19)$$

$$d_{R'P} = \sqrt{(x_R - x_P)^2 + (y_R + y_P)^2 + (z_R - z_P)^2}. \quad (20)$$

### C. Derive EMA's Sensing range model

1) *Weighted CSI Signal Model*: We substitute the optimal normalized weights into Eq. (4), thus weighted CSI signal can be expressed as:

$$\bar{H}(f, t) = \bar{S}(f) + e^{j\theta_{ref}} \sqrt{\sum_{i=1}^{N_{Rx}} |A_i(f, t)|^2} e^{-j2\pi f \frac{d_1(t)}{c}} + \bar{\epsilon}(f, t), \quad (21)$$

where  $N_{Rx}$  is the number of antenna pairs,  $\bar{S}(f)$  is the weighted static component, and  $\bar{\epsilon}(f, t)$  is the weighted thermal noise. Since  $\theta_{ref}$  and the initial phases of  $a_i(f, t)$  do not affect the alignment of dynamic components, they do not impact sensing performance, we can assume them to be zero. So we have  $|A_i(f, t)| = a_i(f, t)$ . Then, we can rewrite Eq. (21) as:

$$\bar{H}(f, t) = \bar{S}(f) + \bar{\epsilon}(f, t) + \sqrt{\sum_{i=1}^{N_{Rx}} \left( \frac{a_i(f, t)}{a_1(f, t)} \right)^2} a_1(f, t) e^{-j2\pi f \frac{d_1(t)}{c}}. \quad (22)$$

By comparing the weighted CSI with the unweighted signal, we can observe that after weighted combining, the dynamic component of the signal is multiplied by a coefficient, which is greater than 1. So weighted combined method has an enhanced effect on dynamic components.

2) *Weighted CSI Influenced by Respiration*: The respiratory behavior of individuals can change the length of dynamic paths. The changes in path length affects both the phase and amplitude of dynamic components. The amplitude is expressed as:

$$\alpha_i(f, t) = \frac{\lambda \sqrt{G_t G_r}}{(4\pi d_i(t))^{\frac{n}{2}}}, \quad (23)$$

where  $\lambda$  is the wavelength of WiFi signal,  $G_t$  and  $G_r$  are antenna gain at the transmitter and the receiver, respectively,  $n$  is path loss factor. Substituting Eq. (23) into Eq. (22) yields:

$$\bar{H}(f, t) = \bar{S}(f) + \frac{\lambda \sqrt{G_t G_r}}{(4\pi)^{\frac{n}{2}}} \sum_{i=1}^{N_{Rx}} \frac{e^{-j2\pi f \frac{d_1(t)}{c}}}{d_i(t)^{\frac{n}{2}}} + \bar{\epsilon}(f, t). \quad (24)$$

Since  $d_{T'P}$  and  $d_{PR'_i}$  are both much larger than  $d_{AB}$ ,  $d_{BC}$  and  $d_{BD}$  by using Taylor expansion we can transform  $d_i(f_{BR}, t)^{-\frac{n}{2}}$  into:

$$d_i(f_{BR}, t)^{-\frac{n}{2}} = \frac{-nu_{Bi}d_{AB}\sin 2\pi f_{BR}t}{2(d_{T'P} + d_{PR'_i})^{\frac{n}{2}+1}} + \frac{1}{(d_{T'P} + d_{PR'_i})^{\frac{n}{2}}}. \quad (25)$$

Substituting Eq. (25) into Eq. (24) yields the combined CSI signal:

$$\bar{H}(f_{BR}, t) = \bar{S}(f) + \bar{\epsilon}(f, t) + (C_1 \sin 2\pi f_{BR}t + C_2) e^{-j2\pi \frac{f}{c} d_1(f_{BR}, t)}, \quad (26)$$

where  $C_1$  and  $C_2$  are constants:

$$C_1 = \frac{\lambda \sqrt{G_t G_r}}{(4\pi)^{\frac{n}{2}}} \sum_{i=1}^{N_{Rx}} \frac{-nu_{Bi}d_{AB}}{2(d_{T'P} + d_{PR'_i})^{\frac{n}{2}+1}} \quad (27)$$

$$C_2 = \frac{\lambda \sqrt{G_t G_r}}{(4\pi)^{\frac{n}{2}}} \sum_{i=1}^{N_{Rx}} \frac{1}{2(d_{T'P} + d_{PR'_i})^{\frac{n}{2}}}. \quad (28)$$

3) *Derive Sensing Range Model*: Eq. (26) successfully characterizes how respiration affects the weighted CSI. The derivation of the estimated respiration rate is illustrated as following steps.

Firstly, weighted CSI signals are projected onto the I-Q plane. Since  $\bar{S}(f)$  determines the center of the circle on the I-Q plane and does not change with time, we can express it as  $\bar{A}_S e^{j\bar{\theta}_S}$ , where  $\bar{A}_S$  is the amplitude of the static component, and  $\bar{\theta}_S$  is the phase of the static component. The projection of  $\bar{\epsilon}(f, t)$  on the I-axis can be written as  $\epsilon_I(f, t)$ . Then, the I-axis coordinate of  $\bar{H}(f_{BR}, t)$  can be written as:

$$I(f_{BR}, t) = \bar{A}_S \cos \bar{\theta}_S + \epsilon_I(f, t) + (C_1 \sin 2\pi f_{BR}t + C_2) \cos 2\pi \frac{f}{c} d_1(f_{BR}). \quad (29)$$

Similarly, we can obtain the Q-axis coordinates of  $\bar{H}(f_{BR}, t)$ :

$$Q(f_{BR}, t) = \bar{A}_S \sin \bar{\theta}_S + \epsilon_Q(f, t) - (C_1 \sin 2\pi f_{BR}t + C_2) \sin 2\pi \frac{f}{c} d_1(f_{BR}). \quad (30)$$

Subsequently, weighted CSI points on I-Q plane are projected on the optimal direction to amplify its variances. The angle between the optimal projection direction and the I-axis is denoted as  $\theta_{od}$ . The projected CSI is expressed as:

$$H_{EMA}(f_{BR}, t) = I(f_{BR}, t) \cos \theta_{od} + Q(f_{BR}, t) \sin \theta_{od}. \quad (31)$$

Finally, in the frequency domain, the frequency corresponding to the highest amplitude is the estimated respiration rate, which is expressed as:

$$\widehat{f_{BR}} = \arg \max_f FFT(H_{EMA}(f_{BR}, t)). \quad (32)$$

Substituting Eq. (32) into Eq. (12), we have the sensing range model:

$$d_{max} = \max d_{PS} \quad \text{s.t.} \quad \left| \arg \max_f FFT(H_{EMA}(d_{PS}, f_{BR}, t)) - f_{BR} \right| \leq \epsilon_{BR}. \quad (33)$$

### D. Derive DiverSense's Sensing Range Model

The final combined CSI of DiverSense has been presented in Section III-C. However, observing Eq. (10), we find that that after scaling dynamic components is independent of the reflection path distance. In other words, when the distance from the transmitter and receiver to the target changes, the scaled dynamic components always have the same amplitude. So, the respiratory sensing range depends entirely on the noise. Next, according to the detailed expression of the noise, we derive the respiratory sensing range model.

Since  $\alpha_p(f_i, t)$  is much smaller than  $S_q(f_i)$ , we can ignore the item with  $\alpha_p(f_i, t)/S_q(f_i)$ . The more detailed CSI ratio model is rewritten as:

$$\frac{H_p(f_i, t)}{H_q(f_i, t)} \approx \frac{\alpha_p(f_i, t)e^{-j2\pi f_i \frac{d_p(t)}{c}}}{S_q(f_i)} + \frac{S_p(f_i)}{S_q(f_i)} + \frac{\epsilon_p(f_i, t) - \frac{S_p(f_i)}{S_q(f_i)}\epsilon_q(f_i, t)}{S_q(f_i)}. \quad (34)$$

Substituting Eq. (32) into each step of signal alignment algorithm, i.e., Eq. (7) - Eq. (10), we obtain the final combined CSI signal:

$$\begin{aligned} \bar{H}'(t) &= \frac{1}{N_{Rx}} \sum_{i=1}^{N_{Rx}} \frac{e^{-j\theta_{ini,1}}(e^{-j2\pi f_i \frac{\Delta d(t)}{c}} - K)}{K_{dif}} + \\ &\frac{1}{N_{Rx}} \sum_{i=1}^{N_{Rx}} \frac{|S_q(f_i)|(\epsilon_p(f_i, t) \frac{S_p(f_i)}{S_q(f_i)} \epsilon_q(f_i, t))}{K_{dif}|\alpha_p(f_i, t)|S_q(f_i)} e^{-j\theta_i}. \end{aligned} \quad (35)$$

Observed from Eq. (35), when the target is farther away from the transceiver, the amplitude attenuation  $|\alpha_p(f_i, t)|$  is smaller and the noise is amplified.

Next, we analyze the impact of respiration on  $\bar{H}'(t)$ . Similar to deriving the EMA's sensing range model, we write  $\Delta d(t)$  and  $|\alpha_p(f_i, t)|$  as functions about  $f_{BR}$ . According to Eq. (17), we can write  $\Delta d(t)$  as:

$$\Delta d(f_{BR}, t) = u_B d_{AB} \sin 2\pi f_{BR} t. \quad (36)$$

Based on our previous derivation (Eq. (13) - Eq. (20)),  $|\alpha_p(f_i, t)|$  can be written as:

$$|\alpha_p(f_i, t)| = C_{3,i} \sin 2\pi f_{BR} t + C_{4,i}, \quad (37)$$

where

$$C_{3,i} = \frac{\lambda_i \sqrt{G_t G_r}}{(4\pi)^{\frac{n}{2}}} \frac{-nu_B d_{AB}}{2(d_{T'P} + d_{PR'})^{\frac{n}{2}+1}} \quad (38)$$

$$C_{4,i} = \frac{\lambda_i \sqrt{G_t G_r}}{(4\pi)^{\frac{n}{2}}} \frac{1}{2(d_{T'P} + d_{PR'})^{\frac{n}{2}}}. \quad (39)$$

Substituting Eq. (36) and Eq. (37) into Eq. (35) gives the relationship between the combined CSI signal and  $f_{BR}$ :

$$\begin{aligned} \bar{H}'(f_{BR}, t) &= \frac{1}{N} \sum_{i=1}^N \frac{e^{-j\theta_{ini,1}}(e^{-j2\pi f \frac{\Delta d(f_{BR}, t)}{c}} - K)}{K_{dif}} + \\ &\frac{1}{N} \sum_{i=1}^N \frac{|S_2(f_i)|(\epsilon_1(f_i, t) - \frac{S_1(f_i)}{S_2(f_i)}\epsilon_2(f_i, t))}{K_{dif}(C_{3,i} \sin 2\pi f_{BR} t + C_{4,i})S_2(f_i)} e^{-j\theta_i}. \end{aligned} \quad (40)$$

Then the above combined CSI-ratio data is converted into one-dimension data by PCA, as described in DiverSense [23]. The above combined CSI-ratio data has two dimensions (I and Q dimensions). Since the combined CSI-ratio data carries respiration pattern, the converted one-dimension data denoted as  $H_{Diver}(f_{BR}, t)$  also embodies the respiration pattern. In the frequency domain of  $H_{Diver}(f_{BR}, t)$ , the frequency corresponding to the highest amplitude is the estimated respiration rate. Then, we have the sensing range model of DiverSense:

$$\begin{aligned} d_{max} &= \max d_{PS} \\ \text{s.t. } &\left| \arg \max_f FFT(H_{Diver}(d_{PS}, f_{BR}, t)) - f_{BR} \right| \leq \varepsilon_{BR}. \end{aligned} \quad (41)$$

## V. EXTEND THE SENSING RANGE OF RESPIRATORY DETECTION IN NLOS SCENARIO

In this section, we first analyze the most related work. Then, we propose a more precise CSI ratio model, providing a basic model for extending the sensing range of respiratory detection. In order to extend the sensing range, we propose a new respiratory detection system which can rapidly align dynamic components without amplifying noise.

### A. Analysis on the Most Related Work

We selected DiverSense as our analysis object, because it is the most advanced method which can effectively extend the sensing range of respiratory detection. Through analysis, we find two problems that can be further addressed.

1) Amplified noise. In order to maximize the sensing range, the work in [23] attempts to align the dynamic components in all subcarriers. The alignment is fulfilled by scaling the dynamic components. We find that when a dynamic component is amplified by scaling, the corresponding noise is also amplified, as shown in Eq. (9). The amplified noise limits the sensing range of respiratory detection. In NLoS scenario, since the received signal is weaker, the amplified noise has a more negative impact on the sensing range.

2) High Computation Complexity. Aligning dynamic components means that the dynamic components of all subcarriers should have the same phase. Having the same phase prevents dynamic components from canceling each other out when combined, thereby enhancing sensing performance. However, the phases of CSI's dynamic components are always different, so rotating the CSI signals is essential to align the dynamic components. The work in [23] finds that if two dynamic components have the same size, the two dynamic components can be aligned by rotating one of the signals until the distance between the corresponding samples is minimized, which implies the need to traverse every possible angle. The traversal method results in high computation complexity. Assuming the number of angles to traverse is  $M$ , the number of samples is  $N$  and the number of subcarriers is  $K$ , then the computational complexity of the traversal method is  $O(M * N * K)$ .

### B. More Precise CSI Ratio Model

In the existing CSI ratio model [23], which is presented in Eq. (6), the dynamic component in the divisor is ignored,

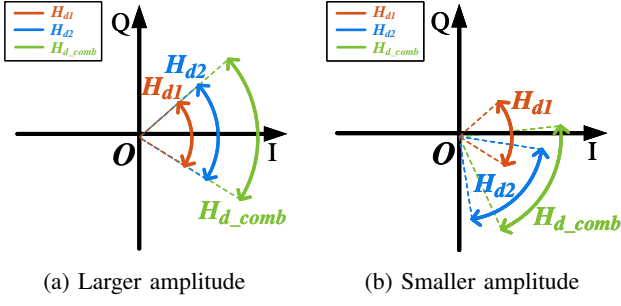


Fig. 4. Integrated dynamic component. (a) shows the integrated dynamic component with larger amplitude. (b) shows the integrated dynamic component with smaller amplitude. But both of them have the same phase change.

because the static component is much larger than the dynamic component. The dynamic component in the dividend is also much smaller than the static component, but it is not ignored. In fact, both of them should not be ignored.

We rewrite the original CSI ratio between two different antenna pairs as:

$$H_{p,q}(f_i, t) = \frac{S_p(f_i) + a_p(f_i, t)D_p(f_i, t) + \epsilon_p(f_i, t)}{S_q(f_i)(1 + \frac{a_q(f_i, t)D_q(f_i, t) + \epsilon_q(f_i, t)}{S_q(f_i)})}, \quad (42)$$

where  $a_p(f_i, t)D_p(f_i, t)$  and  $a_q(f_i, t)D_q(f_i, t)$  are the dynamic components of  $H_p(f_i, t)$  and  $H_q(f_i, t)$ , respectively. Since  $a_q(f_i, t)D_q(f_i, t) + \epsilon_q(f_i, t)$  is much smaller than  $S_q(f_i)$ , we can truncate the Taylor series expansion appropriately:

$$H_{p,q}(f_i, t) \approx \frac{a_p(f_i, t)D_p(t) - \frac{S_p(f_i)}{S_q(f_i)}a_q(f_i, t)D_q(t)}{S_q(f_i)} + \frac{\frac{S_p(f_i)}{S_q(f_i)} + \frac{\epsilon_p(f_i, t) - \frac{S_p(f_i)}{S_q(f_i)}\epsilon_q(f_i, t)}{S_q(f_i)}}{S_q(f_i)}. \quad (43)$$

In the above derivation, we take into account the dynamic components of both  $H_p(f_i, t)$  and  $H_q(f_i, t)$ , rather than simply ignoring the dynamic components of  $H_q(f_i, t)$ . In Eq. (41), the numerator of the first sum term is integrated by the dynamic components of both  $H_p(f_i, t)$  and  $H_q(f_i, t)$ .

We next analyze whether the phase change in the above integrated dynamic component can correctly reveal respiratory feature. First, we have the following consensus. (1) When the transmitter and the receiver are far away from the target, the change in dynamic path distance caused by respiratory is much smaller than the whole dynamic path distance. Therefore, the amplitude of the dynamic component can be considered as a constant with the same magnitude. We have  $a_p(f_i, t) = a_q(f_i, t)$  and we can use  $a(f_i)$  to represent  $a_p(f_i, t)$  and  $a_q(f_i, t)$ . (2) The phase variation of the dynamic components from different subcarriers are similar, as pointed out in [23]. We have  $D_p(f_i, t) = \varphi_p(f)\Delta D(t)$ ,  $D_q(f_i, t) = \varphi_q(f)\Delta D(t)$ , where  $\Delta D(t) = e^{-j2\pi f \frac{\Delta d(t)}{c}}$ ,  $\varphi_p(f)$  and  $\varphi_q(f)$  are not related with the phase change.

On the basis of the above consensus, we can rewrite the integrated dynamic component as:

$$\begin{aligned} & \alpha_p(f_i, t)D_p(f_i, t) - \frac{S_p(f_i)}{S_q(f_i)}\alpha_q(f_i, t)D_q(f_i, t) \\ &= \alpha(f_i)(\varphi_p(f_i) - \frac{S_p(f_i)}{S_q(f_i)}\varphi_q(f_i))\Delta D(t). \end{aligned} \quad (44)$$

According to Eq. (44), the phase change of the integrated dynamic component determined by  $\Delta D(t)$ , can correctly reflect respiratory feature. To simulate the integrated dynamic component of CSI ratio signal, we generate two dynamic components with the same phase change, but different amplitude. As shown in Fig. 4, we rotate one of the dynamic components and observe the integrated dynamic components. The amplitude of the integrated dynamic component in Fig. 4 (a) is larger than that in Fig. 4 (b), but the phase change of the integrated dynamic component is always the same.

### C. RaliSense: a new Respiratory Detection System Based on Rapid Alignment of Dynamic Components

We propose RaliSense, a system that derives change direction vectors of dynamic components to rapidly align dynamic components without amplifying noise. This system is illustrated as follows.

1) *Remove Static Components and Reduce Noise:* Since static component is unrelated to respiration, we remove it before aligning dynamic components. Due to the dynamic components are very small, the distribution of CSI ratio signals on the I-Q plane is mainly determined by the static components and the noise components. The noise determines the distribution range of CSI ratio signals. Since the noise is assumed as a white Gaussian noise with zero mean, the centroid of all projected points of the CSI ratio signal on the I-Q plane can be approximated as the coordinate of the static component on the I-Q plane. The coordinate of the centroid is written as:

$$\left( I_{S_{p,q},f_i}, Q_{S_{p,q},f_i} \right) = \left( \frac{1}{n} \sum_{j=1}^n I_{H_{p,q},f_i}[j], \frac{1}{n} \sum_{j=1}^n Q_{H_{p,q},f_i}[j] \right), \quad (45)$$

where  $I_{H_{p,q},f_i}[j]$  and  $Q_{H_{p,q},f_i}[j]$  are the I-axis coordinates and Q-axis coordinates of the  $j$ -th sample of  $H_{p,q}(f_i, t)$ , respectively. We translate all CSI ratio points which have been projected on the IQ plane make the centroid of these points to be the origin, thus removing the static component. After static component removal, the CSI ratio can be written as:

$$\begin{aligned} \hat{H}_{p,q}(f_i, t) &= \frac{\alpha(f_i)(\varphi_p(f_i) - \frac{S_p(f_i)}{S_q(f_i)}\varphi_q(f_i))\Delta D(t)}{S_q(f_i)} + \\ & \frac{\epsilon_p(f_i, t) - \frac{S_p(f_i)}{S_q(f_i)}\epsilon_q(f_i, t)}{S_q(f_i)}. \end{aligned} \quad (46)$$

Next, we apply the Savitzky-Golay filter [34] to preliminary denoising the CSI ratio signal. The adopted filter is suitable

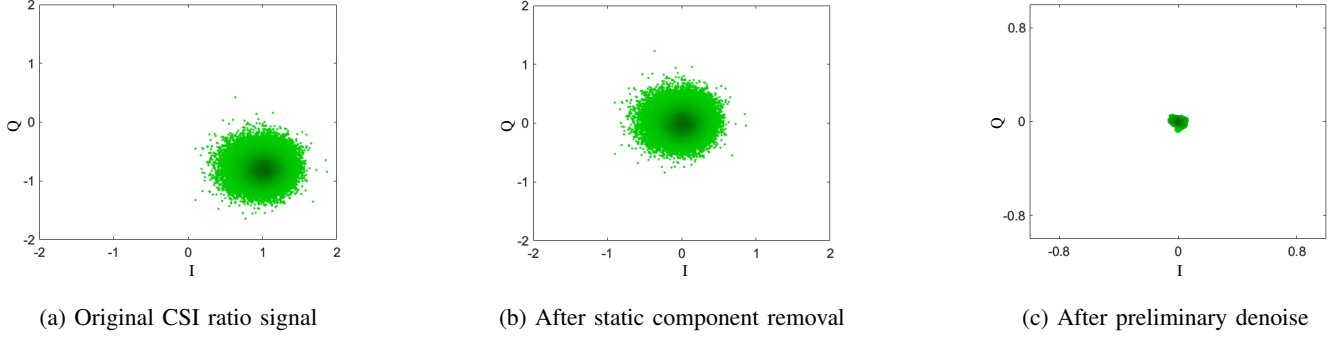


Fig. 5. Effect of static component removal and preliminary denoising. (a) shows original CSI ratio. (b) shows the effect after static component removal. (c) shows the effect after preliminary denoising.

to deal with a variable that is both slowly changing and broken by random noise.

$$\begin{aligned} \tilde{H}_{p,q}(f_i, t) &= \frac{h_t}{2W} \sum_{j=t-W}^{t+W} \hat{H}_{p,q}(f_i, t) \\ &\approx \frac{a(f_i)(\varphi_p(f_i) - \frac{S_p(f_i)}{S_q(f_i)}\varphi_q(f_i))\Delta D(t)}{S_q(f_i)} + \frac{\epsilon'_{p,q}(f_i, t)}{S_q(f_i)}, \end{aligned} \quad (47)$$

where  $2W$  is the window size of the S-G filter,  $\frac{h_t}{2W}$  is the smoothing coefficient, which is obtained by fitting the polynomial by the least squares method. The smoothed noise becomes much smaller. Fig. 5 (c) shows the final effect of static component removal and preliminary denoising. It can be observed that the noise is effectively reduced.

2) *Derive the Change Direction Vector*: In order to align all dynamic components without amplifying noise, we cannot scale the dynamic components. Instead, we propose change direction vector of dynamic components to rapidly align dynamic components. The change direction vector is the direction on which the projected dynamic component has the maximum variance.

When there is no noise, according to Eq. (47) and the expression of  $\Delta D(t)$ , the trajectory of dynamic component is an arc. We call the direction of the maximum variance of the arc as the change direction vector. In this case, the vector is on the line connecting the two endpoints of the arc. The reason is that when the dynamic component is projected in this direction, the length of the projected dynamic component is the longest. As shown in Fig. 6, if the dynamic component is projected in another direction ( $A'B'$  in Fig. 6), the length of the projected dynamic component becomes shorter.

When the noise is taken into consideration, the dynamic component affected by the noise can be regarded as an arc belt, as show in Fig. 7. The direction of the maximum variance of the arc belt is the change direction vector of the noisy dynamic components. Next, we derive the expression of the change direction vector.

The most important feature of the change direction vector is that it represents the direction on which the projected dynamic component has the maximum variance. Based on its feature,

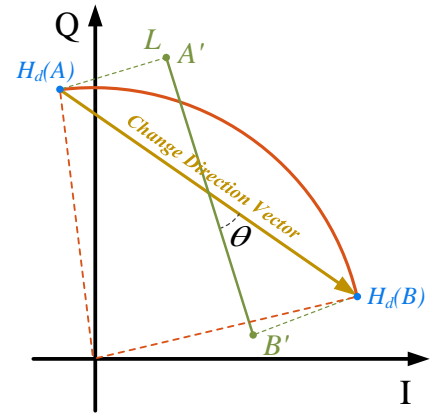


Fig. 6. Change direction vector of dynamic components without noise.

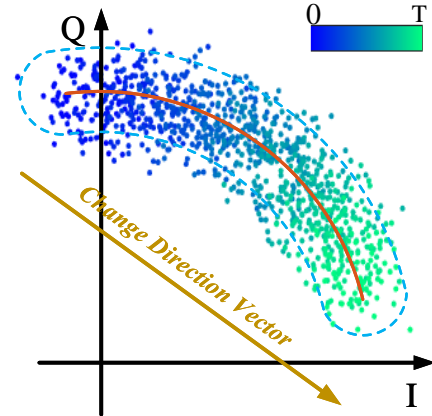


Fig. 7. Change direction vector of dynamic components with noise.

we first construct the covariance matrix of noisy dynamic component as:

$$\mathbf{C}_{p,q,f_i} = \begin{pmatrix} \text{cov}(I_{H_{p,q},f_i}, I_{H_{p,q},f_i}) & \text{cov}(I_{H_{p,q},f_i}, Q_{H_{p,q},f_i}) \\ \text{cov}(Q_{H_{p,q},f_i}, I_{H_{p,q},f_i}) & \text{cov}(Q_{H_{p,q},f_i}, Q_{H_{p,q},f_i}) \end{pmatrix}, \quad (48)$$

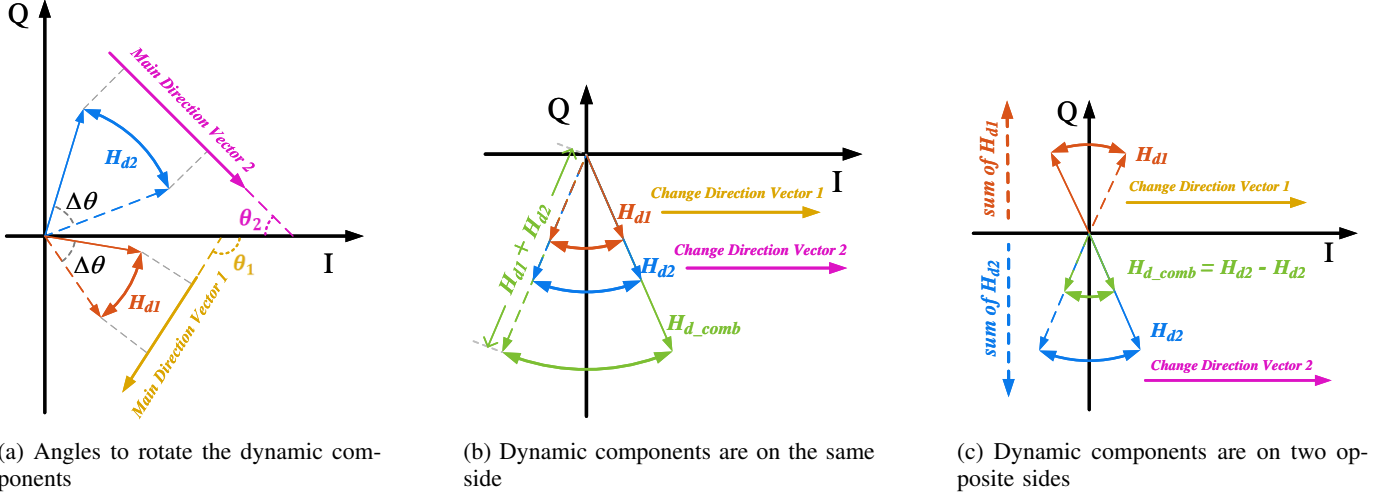


Fig. 8. Determine rotation angle by the polarity of CSI ratio sum. (a) shows the angles to rotate dynamic components. (b) shows the dynamic components on the same side after rotating. (c) shows the dynamic components on two opposite sides after rotating.

where

$$\text{cov}(I_{H_{p,q,f_i}}, Q_{H_{p,q,f_i}}) = \frac{1}{N} \sum_{i=1}^N (I_{H_{p,q,f_i}}[i] - \bar{I}_{H_{p,q,f_i}})(Q_{H_{p,q,f_i}}[i] - \bar{Q}_{H_{p,q,f_i}}), \quad (49)$$

where  $N$  is the number of CSI ratio samples, and  $\bar{I}_{H_{p,q,f_i}}$  and  $\bar{Q}_{H_{p,q,f_i}}$  are the means of  $I_{H_{p,q,f_i}}$  and  $Q_{H_{p,q,f_i}}$ , respectively.

Then, the eigendecomposition is used to calculate the eigenvalues and eigenvectors of the covariance matrix. As proved in [35], the eigenvector of the covariance matrix, which corresponds to the largest eigenvalue, is the direction of the maximum variance. So, the eigenvector corresponding to the largest eigenvalue is the change direction vector. The largest eigenvalue is expressed as:

$$\lambda_{p,q,f_i} = \max(\lambda_i), \text{ s.t. } \det(\mathbf{C}_{p,q,f_i} - \lambda_i \mathbf{E}) = 0, \quad (50)$$

where  $\lambda_i$  represents the eigenvalues of  $\mathbf{C}_{p,q,f_i}$ ,  $\mathbf{E}$  represents the identity matrix. By transforming the above equation, we can finally obtain the expression of the change direction vector as:

$$\mathbf{v}_{p,q,f_i} = \left( \text{cov}(Q_{H_{p,q,f_i}}, I_{H_{p,q,f_i}}), \lambda_{p,q,f_i} - \text{cov}(I_{H_{p,q,f_i}}, I_{H_{p,q,f_i}}) \right)^T. \quad (51)$$

3) *Determine Rotation Angle by the Polarity of CSI Ratio Sum:* Simply rotating the CSI ratios based on the change direction vectors cannot align all dynamic components. As shown in Fig. 8 (a), according to the derivation in Section V-C, the change direction vectors of these two dynamic components are calculated. Then based on the angle between the change direction vector and the I-axis, the rotation angles for aligning the change direction vectors can be obtained, which are  $\theta_1$  and  $\theta_2$ , respectively. After rotating the dynamic components, they are aligned theoretically, i.e., they are all above or below the I-axis. As shown in Fig. 8(b), both dynamic components

are below the I-axis, where  $H_{d\_comb} = H_{d1} + H_{d2}$ . However, in practice, after the rotation the dynamic components may be on two opposite sides. For example, as shown in Fig. 8(c), although the change direction vectors are parallel to the I-axis, the combined dynamic component is weakened, i.e.,  $H_{d\_comb} = H_{d2} - H_{d1}$ . In this case, the two dynamic components are not aligned.

To solve the above rotation angle ambiguity problem, we adjust rotation angle by the polarity of the ratio signal sum. The main idea of rotation angle adjustment is described by an example from Fig. 8(c). The sums of  $H_{d1}$  and  $H_{d2}$  are first calculated, respectively. Since the samples of  $H_{d1}$  are all above the I-axis, the sum of  $H_{d1}$  is above the I-axis, while  $H_{d2}$  is the opposite. We rotate the dynamic component whose sum is above the I-axis by 180 degrees. The dynamic components will be aligned below the I-axis. The specific steps are as follows.

(1) *The sum of rotated CSI ratio signals.* After rotating CSI ratio signals based on change direction vector, we calculate the sum of ratio signals:

$$ss_{p,q,f_i} = \sum_{t=1}^T \tilde{H}_{p,q}(f_i, t) e^{j \arctan \mathbf{v}_{p,q,f_i}}, \quad (52)$$

where  $ss_{p,q,f_i}$  is the sum of samples of  $\tilde{H}_{p,q}(f_i, t)$ , which is a complex value, and  $\arctan \mathbf{v}_{p,q,f_i}$  represents the rotation angle between the change direction vector and I-axis.

(2) *Rotation angle adjustment.* We judge the polarity of rotated CSI ratio sum based on the imaginary part of rotated ratio. In this paper, without loss of generality, we align all dynamic components and make them aligned below I-axis. When  $ss_{p,q,f_i}$  is above the I-axis, we need to rotate  $\tilde{H}_{p,q}(f_i, t)$  by an additional 180 degrees. Based on the polarity of CSI ratio sum, we get the rotation angles:

$$\theta_{p,q,f_i} = \arctan \mathbf{v}_{p,q,f_i} + \pi \left[ \frac{\text{Im}(ss_{p,q,f_i})}{2 |\text{Im}(ss_{p,q,f_i})|} \right], \quad (53)$$

where  $\text{Im}(ss_{p,q,f_i})$  is the imaginary part of  $ss_{p,q,f_i}$ .

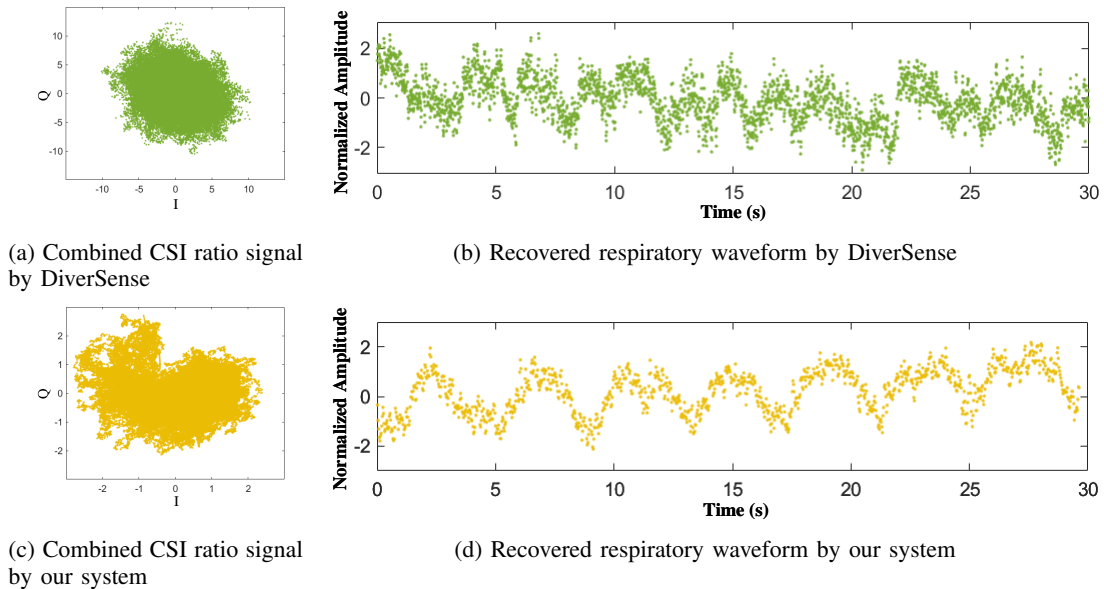


Fig. 9. Combined CSI ratio signal and respiratory waveform by DiverSense and our system. (a) and (c) show the combined CSI ratio signals by DiverSense and our system, respectively. (b) and (d) show the recovered respiratory waveforms by DiverSense and our system, respectively.

(3) *Combining all CSI ratio signals.* Since we have obtained the rotation angles for all CSI ratio signals, we can align all dynamic components by rotating CSI ratio signals. Then, the rotated CSI ratios are combined, which is expressed as:

$$\bar{H}(t) = \sum_{p=1}^{M_{Rx}} \sum_{q=1, q \neq p}^{M_{Rx}} \sum_{i=1}^K \tilde{H}_{p,q}(f_i, t) e^{j\theta_{p,q, f_i}}, \quad (54)$$

Assuming the number of samples is  $N$  and the number of subcarriers is  $K$ , then the computational complexity of our alignment method is  $O(N * K)$ .

In the frequency domain of  $\bar{H}(t)$ , the frequency corresponding to the highest amplitude is the estimated respiration rate. Then, we have the sensing range model of our system:

$$\begin{aligned} d_{max} &= \max d_{PS} \\ \text{s.t. } & \left| \arg \max_f FFT(\bar{H}(d_{PS}, t)) - f_{BR} \right| \leq \epsilon_{BR}. \end{aligned} \quad (55)$$

We use real experimental results obtained at a NLoS sensing range of 5 m to verify the effectiveness of our algorithms. We detect the target's respiration by DiverSense and our method, respectively. The results of combining CSI ratios by DiverSense and our method are shown in Fig. 9 (a) and (c), respectively. Based on previous analysis, dynamic components affected by the noise should look like an arc belt, because the phase change of dynamic components varies in accord with respiration. An arc belt like shape can be observed in Fig. 9 (c), showing that the combined CSI ratio by our method can reflect the phase change of dynamic components. On the contrary, the combined CSI ratio in Fig. 9 (a) can hardly reflect the phase change of dynamic components. As a result, compared to the recovered respiratory waveform in Fig. 9 (b), the recovered waveform in Fig. 9 (d) can better reflect the real respiratory waveform.

TABLE I: Simulation Parameters

Parameter	Value	Parameter	Value
$f_0$	5.2 GHz	$d_{BC}$	0.5 m
$n$	3	$d_{CD}$	0.1 m
$\sigma_{ratio}$	0.3	$d_{FG}$	no more than 6 m
$Fs$	2000 Hz	$d_{FE}$	no more than 6 m
$f_{BR}$	0.25 Hz	$d_{R'E}$	no more than 6 m
$\epsilon_{BR}$	0.02	$d_{T'G}$	no more than 6 m
$d_{AB}$	10 mm	$d_{PF}$	no more than 6 m

## VI. EVALUATION AND ANALYSIS

In this section, we conduct comprehensive experiments to evaluate the effectiveness of our derived respiratory sensing range models and our proposed respiratory detection system.

### A. Simulation and Analysis

The main simulation parameters for respiratory detection in NLoS scenario are shown in Table 1. These parameters have been defined in previous sections. The path loss factor is set to 3 for the NLoS scenario [36]. The noise of CSI ratio, i.e. the noise item in Eq. 6, is white Gaussian noise with a standard deviation denoted as  $\sigma_{ratio}$ . According to real CSI measurements,  $\sigma_{ratio}$  is set to 0.3. The sampling rate for collecting CSI samples at the receiver is set to 2000 Hz. Generally, human respiratory rates range from 0.1 to 0.5 Hz [37]. Here, we set the respiratory rate of the target to 0.25 Hz. The displacement of the chest is usually between 5 mm and 12 mm [23], which we set to 10 mm. The error threshold is set to 0.02. The parameters related to the positions of the transmitter, receiver, and target are set to no more than 6 meters.

We substitute the values of parameters into the sensing range model of the respective methods, and adjust the values of distance parameters to simulate the target moving away from the sensing devices. As shown in Fig. 10, we obtain

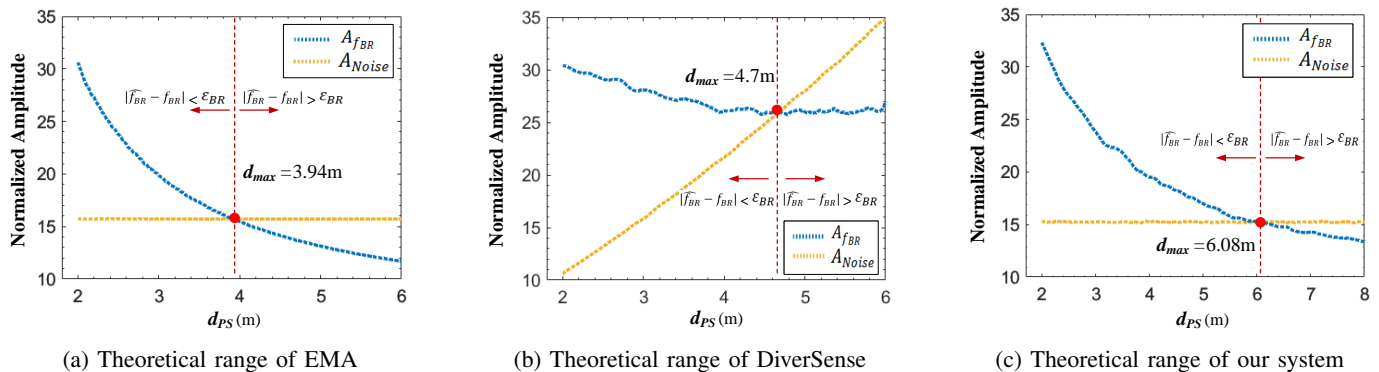


Fig. 10. Theoretical sensing ranges of EMA, DiverSense and our system.

the theoretical sensing ranges corresponding to three systems, i.e., EMA, DiverSense and our system. The theoretical sensing range of respiratory detection for EMA, DiverSense and our system are 3.94 m, 4.70 m, and 6.08 m, respectively. In Fig. 10,  $A_{f_{BR}}$  represents the maximum amplitude within the respiratory frequency band (0.1 ~ 0.5 Hz), while  $A_{noise}$  is the maximum amplitude outside the respiratory frequency band. In the simulation, we find that the frequency corresponding to  $A_{f_{BR}}$  is very close to the real respiratory rate. When  $A_{f_{BR}}$  is greater than  $A_{noise}$ ,  $\hat{f}_{BR}$  is very close to the real respiratory rate and the breathing rate estimation error is smaller than  $\epsilon_{BR}$ . Otherwise,  $\hat{f}_{BR}$  is the frequency corresponding to  $A_{noise}$  and the breathing rate estimation error should be bigger than  $\epsilon_{BR}$ . As shown in Fig. 10, as the distance between the target and sensing device increases,  $A_{f_{BR}}$  decreases while  $A_{noise}$  increases or keeps unchanged. When  $A_{f_{BR}}$  is larger than  $A_{noise}$ , the estimation error is smaller than  $\epsilon_{BR}$ . Once  $A_{f_{BR}}$  falls below  $A_{noise}$ , the estimation error becomes larger than  $\epsilon_{BR}$ . The distance  $d_{PS}$  corresponding to the intersection of  $A_{f_{BR}}$  and  $A_{noise}$  is the theoretical sensing range.

However, we find a gap between our simulation result and previous work's experimental result [22], [23]. The main reason is illustrated as follows. Firstly, in our scenario, the target is lying on his back, where the chest is not directly facing the transmitter and receiver. Consequently, when the chest displacement is 10 mm, the change of dynamic path length in our scenario is only about 2.5 mm according to Eq. (17). In contrast, in previous work [22], [23], where the chest is directly facing the transmitter and receiver, the change of dynamic path length is 20 mm. It is clear that the change of dynamic path length in our scenario is much smaller. Thus, the smaller change of dynamic path length leads to a smaller phase change, which is more easily overwhelmed by noise, thereby reducing the sensing range for respiratory detection.

In Fig. 10 (a) and (c), as the distance between the target and sensing device increases,  $A_{f_{BR}}$  corresponding to EMA and our system decreases, while  $A_{noise}$  almost unchanged. For this phenomenon, we offer the following explanation. According to Eq. (24) and Eq. (47), the amplitude of the dynamic component in the CSI model corresponding to EMA and our method is negatively correlated to the distance between the target and sensing device. Therefore,  $A_{f_{BR}}$  will decrease as

the target is farther away from the sensing devices. Since the noise component is independent of the distance,  $A_{noise}$  keeps almost unchanged.

In Fig. 10 (b), as the distance between the target and sensing device increases,  $A_{f_{BR}}$  corresponding to DiverSense slightly decreases, while  $A_{noise}$  increases. The reason is explained as follow. According to Eq. (36), the range of phase variation of the dynamic component is negatively correlated to the distance between the target and the sensing device. The decrease in the range of phase variation leads to decrease of the amplitude of the reconstructed respiratory waveform, resulting in a decrease in  $A_{f_{BR}}$ . According to Eq. (35), when the target is farther away from the sensing device, the amplitude attenuation is smaller and the noise is amplified, resulting in an increase in  $A_{noise}$ .

## B. Experimental Settings

The sensing devices consists are a pair of WiFi transceivers equipped with low-cost Intel 5300 WiFi cards, in which working frequency is 5.24 GHz and all the antennas are omnidirectional. We install it in commercial computing devices such as miniPC. The devices each have a 4GB RAM and a Celeron J3060 Processor up to 2.48 GHz. The hardware performance is similar or even inferior to some commercial WiFi APs such as ASUS RT-BE88U. The sampling rate is the same with the simulation settings, both at 2000 Hz. We recruit 8 volunteers (i.e., 4 males and 4 females) and all the targets breath normally. We use the Neulog respiration monitor belt to obtain ground truth for performance evaluation.

Fig. 11 (a) shows the layout of our experimental scene. We place the sensing devices on the same side of the target and place a 5cm-thick solid wooden screen between the target and the transceiver as an obstacle. In Fig. 11 (b), the target lies on a bed which is 0.7 m higher than that in Scenario 1. The target lies in a different orientation which is opposite to Scenario 1. The obstacle is a 10cm-thick solid wooden screen, double thicker than that in Scenario 1. Since the working frequency of WiFi signal in this paper is around 5.24 GHz, according to attenuation rates of different materials in [38], the WiFi signal experiences significant attenuation as large as 22 dB when penetrating the obstacle. The penetration loss is so large that the LoS signal can be regarded to be blocked by the obstacle.

We collect CSI data and detect respiration by EMA, DiverSense and our system. If the difference between the detected respiratory rate and the real respiratory rate does not exceed  $\epsilon_{BR}$ , the respiration rate is supposed to be correctly detected. In this case, the distance between the target and sensing device is still smaller than the maximum sensing range, i.e., the sensing range has not yet been reached. Then, the target moves further away from the sensing devices, and the detection of respiratory rate is conducted again. The maximum distance between the target and sensing device satisfying correct detection of respiration rate is recorded as the maximum sensing range.



(a) Experiment Scenario 1



(b) Experiment Scenario 2

Fig. 11. Indoor NLoS experiment scenarios.

### C. Experiment Results

1) *Comparison of Respiratory Waveforms by Different Systems:* We compare the respiratory waveforms of EMA, DiverSense and our system at distances of 2 m, 4 m and 6 m, respectively. The respiratory waveforms are shown in the Fig. 12. The four waveforms in the left-most column of Fig. 12 shows that all the three systems can accurately detect respiration in NLoS scenario when the direct distance between the target and sensing device is 2 m. However, when the direct distance between the target and sensing device increases to 4 m, as shown in the middle column of Fig. 12, the waveform constructed by EMA is obviously different from the real respiratory waveform, while the waveforms constructed by DiverSense and our system still match the ground truth. It shows the superiority of DiverSense and our system over EMA at the sensing distance of 4 m.

If the distance between the target and sensing device is further increased to as long as 6 m, as shown in the right-

most column of Fig. 12, the waveforms constructed by EMA and DiverSense are both significantly different from the real respiratory waveform, while our system can still achieve accurate respiratory detection. Although the respiratory waveform obtained by DiverSense still presents periodic variation, the variation frequency is obviously much higher than the real respiratory rate, which can be observed by comparing the waveform of DiverSense with the ground truth. The above phenomenon demonstrates the superiority of our system at a long sensing distance in NLoS scenario.

2) *Comparison of Theoretical and Practical Sensing Ranges in Different Tx-Rx Distances:* In order to verify the effectiveness of our derived sensing range model, we evaluate whether the theoretical sensing range by our derived model is consistent with the real sensing range obtained by practical respiratory detection system. Since we have built sensing range models for EMA, DiverSense and our system, the effectiveness of all the three sensing range models will be verified. In the experiment, we change the  $Tx-Rx$  distance (i.e., the distance between the transmitter and receiver) from 2 m to 4 m, so that the influence of the  $Tx-Rx$  distance on both the theoretical and practical sensing ranges can be investigated.

The theoretical and practical sensing ranges in different  $Tx-Rx$  distances are shown in Fig. 13. We can observe that the theoretical sensing range of each respiratory detection system is always close to the corresponding practical sensing range, no matter how the  $Tx-Rx$  distance changes. The differences between the theoretical and practical sensing ranges are 0.184 m, 0.165 m and 0.188 m, for EMA, DiverSense and our system, respectively. It is noted that each of the aforementioned differences is actually averaged on  $Tx-Rx$  distances. It shows that the theoretical sensing ranges derived by our proposed models are always consistent with the real sensing ranges. So the effectiveness of our derived sensing range models is demonstrated.

For each of the three respiratory detection systems, when the  $Tx-Rx$  distance increases, the theoretical and practical sensing ranges in the NLoS scenario both become shorter, as shown in Fig. 13. The reason is explained as follow. When the distance between the transmitter and receiver increases, the length of NLoS dynamic propagation path also increases, weakening the dynamic components of CSI and thus reducing the sensing ranges of each respiratory detection system.

It can also be observed that our system always has the longest theoretical and practical sensing ranges, no matter how the  $Tx-Rx$  distance changes. The theoretical sensing range of our system is 24.8% and 67.3% larger than DiverSense and EMA, while the practical sensing range of our system is 22.7% and 66.0% larger than DiverSense and EMA, respectively. It is noted that each of the calculation results is already averaged on  $Tx-Rx$  distances.

3) *The Impact of Different Environments:* We also conduct experiments in a different room (Scenario 2 shown in Fig. 11 (b)) to justify the effectiveness of our proposed model in different environments. Compared with Scenario 1 in Fig. 11 (a), the bed in Scenario 2 is 0.7 m higher and the room has a different arrangement of the furniture. As shown in Fig. 14, we can observe that, regardless of changes in the Tx-

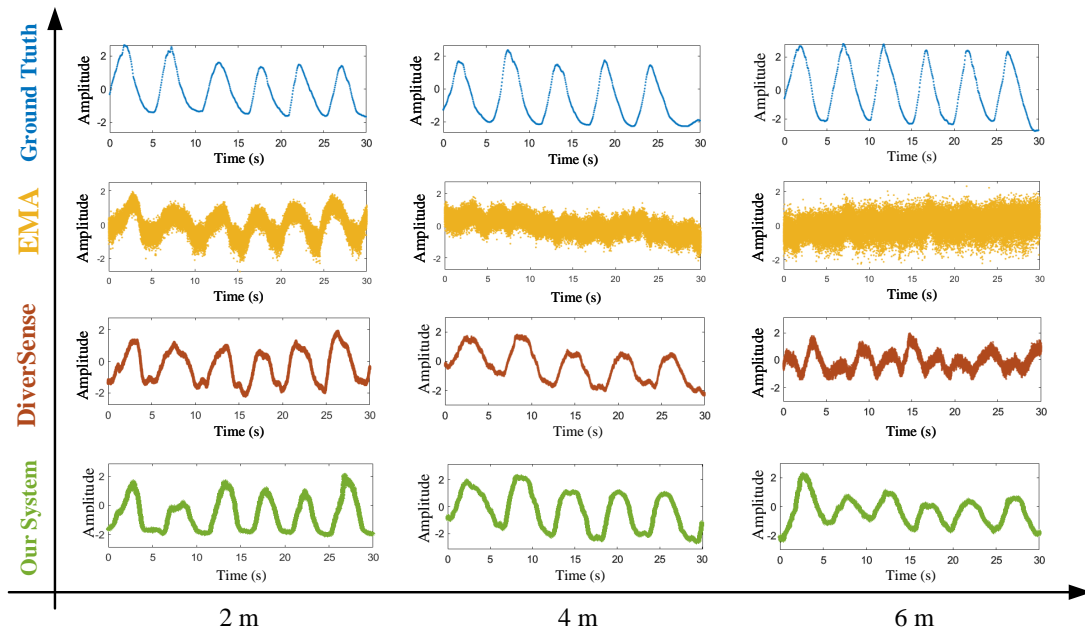


Fig. 12. Respiratory waveforms recovered by EMA, DiverSense and our system.

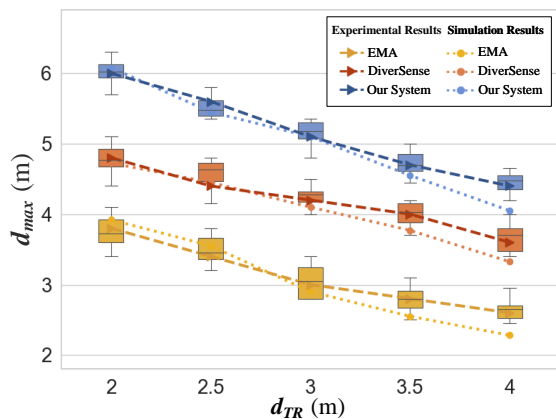


Fig. 13. Theoretical and practical sensing ranges in different  $T_x$ - $R_x$  distances.

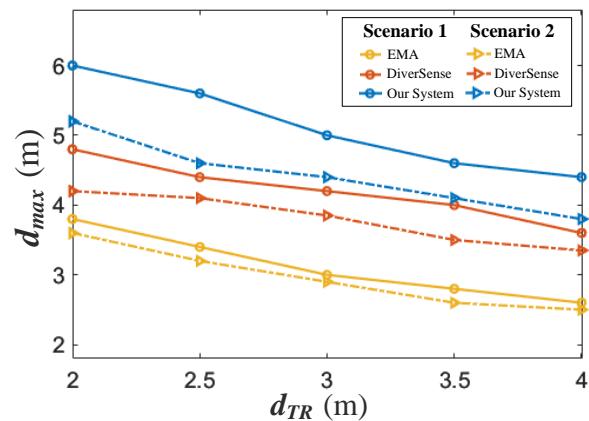


Fig. 14. Practical sensing ranges in different environments.

Rx distance, the practical sensing ranges in Scenario 2 are shorter than those in Scenario 1. The reason is explained as follow. In Scenario 2, the target lies on a higher bed. According to Eq. (17), the change of dynamic path length in Scenario 2 is smaller than that in Scenario 1, resulting in a smaller change of the phase in dynamic component. Then the phase change of dynamic component is more likely to be smaller than that of noise, especially when the target is far away from sensing devices. Consequently, the sensing range of respiratory detection is reduced. It can also be observed that, in different NLoS scenarios, our system always has the longest practical sensing ranges, no matter how the  $T_x$ - $R_x$  distance changes.

4) *The Impact of Different Targets*: In this experiment, we investigate the impact of targets with different body sizes and genders on respiratory sensing range. The targets are four females and four males. Their heights range from 156 cm to

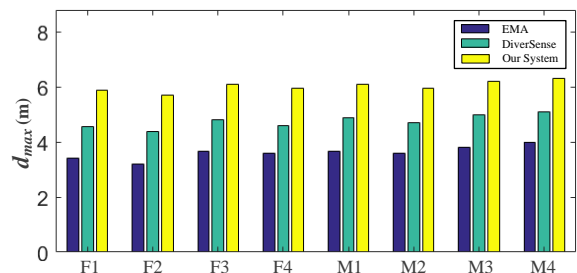
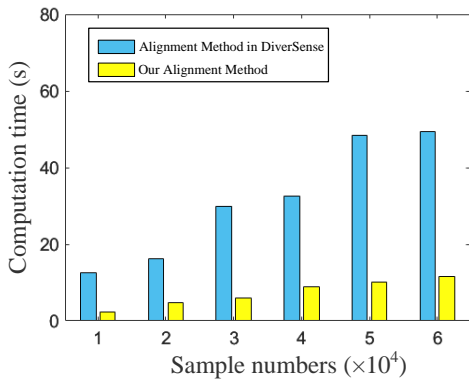
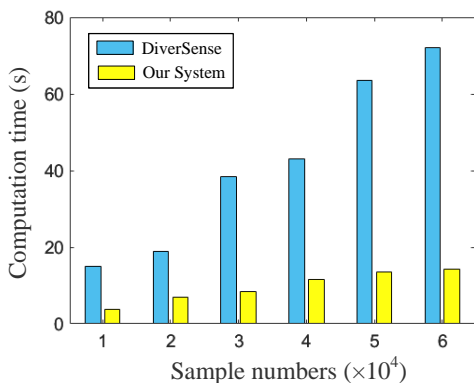


Fig. 15. Practical sensing ranges of different targets by different respiratory detection systems.

187 cm, while their weights range from 45 kg to 79 kg. For each target, we record ten groups of 5-min WiFi respiratory sensing data.



(a) Computation time of different alignment methods



(b) Computation time of DiverSense and our system

Fig. 16. Computation time of alignment methods and respiratory detection systems.

Fig. 15 shows the practical sensing ranges of different targets by different respiratory detection systems. Obviously, the sensing ranges of the eight targets are different from each other due to significant physical differences among the targets. For example, the sensing range differences between F2 and M4 are 0.8 m, 0.7 m and 0.6 m, for EMA, DiverSense, and our system, respectively. Clearly, the sensing ranges of above systems are all influenced by the physical differences. Among these systems, the EMA is the most significantly affected by such differences, while our system is the least affected. This demonstrates that our system has better sensing range robustness for different targets compared to EMA and DiverSense.

We also calculate the average sensing range for female and male targets, respectively. As to EMA, DiverSense and our system, the average sensing ranges of the four female targets are 3.46 m, 4.56 m and 5.88 m, respectively, while those of the four male targets are 3.76 m, 4.95 m and 6.13 m, respectively. Obviously the average sensing range of the male targets is larger than the female targets. The reason is that female targets normally have smaller chest movement and smaller body size, weakening the amplitude and phase change of CSI dynamic components and thus reducing the sensing range.

5) *Computational Complexity*: One major motivation of our work is to reduce the computational complexity of DiverSense which has achieved the maximum sensing range among existing work. The computational complexity of DiverSense mainly comes from the alignment of dynamic components, because it requires traversing all possible rotation angles to find the best rotation angle. Our system is supposed to have lower complexity, because we can align dynamic components without the traversal on all possible rotation angles. Experiments are conducted to verify whether our proposed alignment method can really reduce the complexity of dynamic component alignment method in DiverSense. The results are shown in Fig. 16 (a). It can be observed that the computation time of our method is much shorter than that of the alignment method in DiverSense. Although the computation time of the two alignment methods both increases with the number of CSI samples, our method always run faster than the method in DiverSense. On average, the computation time of our alignment method is only 23.7% of the alignment method in DiverSense.

Fig. 16 (b) shows the whole computation time of EMA, DiverSense and our system. Comparing Fig. 16 (a) and Fig. 16 (b), we can find that the alignment method in DiverSense makes up 77.5% of the whole computation time of DiverSense, validating that the complexity of DiverSense is mainly from the alignment of dynamic components. The percentage value is averaged at different CSI sample numbers. Observed From Fig. 16 (b), the computational complexity of our system is much lower than that of DiverSense. The average computation time of our system at different CSI sample numbers is only 25.1% of the computation time of DiverSense. Although EMA has the lowest complexity, its respiratory detection accuracy and respiratory sensing range are both much lower than DiverSense and our system, according to previous analysis.

## VII. CONCLUSION

Blocked by obstacles in NLoS scenarios, WiFi signals reflected from human target become much weaker and limit the sensing range. In the existing best respiratory detection system, the scaling of dynamic components causes noise amplification and the alignment of dynamic components increases computation complexity. To solve the above problems, we first model WiFi sensing range for respiratory detection in NLoS scenario, and then design a new respiratory detection system called RaliSense. Our system can further extend the NLoS sensing range in lower computation complexity. RaliSense first removes static components and reduces noise, then derives the change direction vector of dynamic components, determines rotation angle by the polarity of CSI ratio sum, and finally combines all rotated CSI ratio signals. Based on the change direction vector and CSI ratio sum polarity, the rotation angle for aligning dynamic components can be quickly calculated, so that dynamic components can be rapidly aligned without amplifying noise. Extensive simulation and experiment results verify the effectiveness of our proposed sensing range models and demonstrate the superiority of our proposed system. Our system can extend the NLoS sensing range by 22.7% compared to the best existing work, and spend only 25.1% of computation time.

## REFERENCES

- [1] Kamran Ali, Mohammed Alloulah, Fahim Kawsar, and Alex X Liu. On goodness of wifi based monitoring of sleep vital signs in the wild. *IEEE Transactions on Mobile Computing*, 22(1):341–355, 2021.
- [2] Jiefan Qiu, Pan Zheng, Kaikai Chi, Ruiji Xu, and Jiajia Liu. Respiration monitoring in high-dynamic environments via combining multiple wifi channels based on wire direct connection between rx/tx. *IEEE Internet of Things Journal*, 10(2):1558–1573, 2022.
- [3] Feng Zhang, Chenshu Wu, Beibei Wang, Min Wu, Daniel Bugos, Hangfang Zhang, and KJ Ray Liu. Smars: Sleep monitoring via ambient radio signals. *IEEE Transactions on Mobile Computing*, 20(1):217–231, 2019.
- [4] Yuqing Yin, Xu Yang, Jie Xiong, Sunghoon Ivan Lee, Pengpeng Chen, and Qiang Niu. Ubiquitous smartphone-based respiration sensing with wi-fi signal. *IEEE Internet of Things Journal*, 9(2):1479–1490, 2021.
- [5] Zhengxin Guo, Wenyang Yuan, Linqing Gui, Biyun Sheng, and Fu Xiao. Breatheband: a fine-grained and robust respiration monitor system using wifi signals. *ACM Transactions on Sensor Networks*, 19(4):1–18, 2023.
- [6] Yuhan Pan, Zhipeng Zhou, Wei Gong, and Yuguang Fang. Sat: A selective adversarial training approach for wifi-based human activity recognition. *IEEE Transactions on Mobile Computing*, 2024.
- [7] Dan Wu, Ruiyang Gao, Youwei Zeng, Jinyi Liu, Leye Wang, Tao Gu, and Daqing Zhang. Fingerdraw: Sub-wavelength level finger motion tracking with wifi signals. *Proceedings of the ACM on Interactive, Mobile, Wearable and Ubiquitous Technologies*, 4(1):1–27, 2020.
- [8] Kai Niu, Fusang Zhang, Xuanzhi Wang, Qin Lv, Haitong Luo, and Daqing Zhang. Understanding wifi signal frequency features for position-independent gesture sensing. *IEEE Transactions on Mobile Computing*, 21(11):4156–4171, 2021.
- [9] Mohamed Hany Mahmoud, Shamman Noor Shoudha, Mohamed Abdallah, and Naofal Al-Dhahir. Openpose-inspired reduced-complexity csi-based wifi indoor localization. *IEEE Communications Letters*, 2024.
- [10] Jingxue Bi, Jianhui Wang, Hongji Cao, Guobiao Yao, Yunjia Wang, Zengke Li, Meng Sun, Hongchao Yang, Jie Zhen, and Guoqiang Zheng. Inverse distance weight-assisted particle swarm optimized indoor localization. *Applied Soft Computing*, 164:112032, 2024.
- [11] Zheng Yang, Yi Zhang, and Qian Zhang. Rethinking fall detection with wi-fi. *IEEE Transactions on Mobile Computing*, 2022.
- [12] Sijie Ji, Yaxiong Xie, and Mo Li. Sifall: Practical online fall detection with rf sensing. In *Proceedings of the 20th ACM Conference on Embedded Networked Sensor Systems*, pages 563–577, 2022.
- [13] Xuanzhi Wang, Kai Niu, Anlan Yu, Jie Xiong, Zhiyun Yao, Junzhe Wang, Wenwei Li, and Daqing Zhang. Wimeasure: Millimeter-level object size measurement with commodity wifi devices. *Proceedings of the ACM on Interactive, Mobile, Wearable and Ubiquitous Technologies*, 7(2):1–26, 2023.
- [14] Ruiqi Kong and He Chen. Csi-rff: Leveraging micro-signals on csi for rf fingerprinting of commodity wifi. *IEEE Transactions on Information Forensics and Security*, 19:5301–5315, 2024.
- [15] Wanguo Jiao and Changsheng Zhang. An efficient human activity recognition system using wifi channel state information. *IEEE Systems Journal*, 17(4):6687–6690, 2023.
- [16] Linqing Gui, Wenyang Yuan, and Fu Xiao. Csi-based passive intrusion detection bound estimation in indoor nlos scenario. *Fundamental Research*, 3(6):988–996, 2023.
- [17] Fusang Zhang, Daqing Zhang, Jie Xiong, Hao Wang, Kai Niu, Beihong Jin, and Yuxiang Wang. From fresnel diffraction model to fine-grained human respiration sensing with commodity wi-fi devices. *Proc. ACM Interact. Mob. Wearable Ubiquitous Technol.*, 2(1), March 2018.
- [18] Daqing Zhang, Hao Wang, and Dan Wu. Toward centimeter-scale human activity sensing with wi-fi signals. *Computer*, 50(1):48–57, 2017.
- [19] Jinyi Liu, Youwei Zeng, Tao Gu, Leye Wang, and Daqing Zhang. Wi-phone: Smartphone-based respiration monitoring using ambient reflected wifi signals. *Proceedings of the ACM on Interactive, Mobile, Wearable and Ubiquitous Technologies*, 5(1):1–19, 2021.
- [20] Xuyu Wang, Chao Yang, and Shiwen Mao. Phasebeat: Exploiting csi phase data for vital sign monitoring with commodity wifi devices. In *2017 IEEE 37th International Conference on Distributed Computing Systems (ICDCS)*, pages 1230–1239. IEEE, 2017.
- [21] Youwei Zeng, Dan Wu, Jie Xiong, Enze Yi, Ruiyang Gao, and Daqing Zhang. Farsense: Pushing the range limit of wifi-based respiration sensing with csi ratio of two antennas. *Proceedings of the ACM on Interactive, Mobile, Wearable and Ubiquitous Technologies*, 3(3):1–26, 2019.
- [22] Youwei Zeng, Jinyi Liu, Jie Xiong, Zhaopeng Liu, Dan Wu, and Daqing Zhang. Exploring multiple antennas for long-range wifi sensing. *Proceedings of the ACM on Interactive, Mobile, Wearable and Ubiquitous Technologies*, 5(4):1–30, 2021.
- [23] Yang Li, Dan Wu, Jie Zhang, Xuhai Xu, Yaxiong Xie, Tao Gu, and Daqing Zhang. Diversense: Maximizing wi-fi sensing range leveraging signal diversity. *Proceedings of the ACM on Interactive, Mobile, Wearable and Ubiquitous Technologies*, 6(2):1–28, 2022.
- [24] Dongheng Zhang, Yang Hu, and Yan Chen. Breath status tracking using commodity wifi. In *2018 IEEE Global Communications Conference (GLOBECOM)*, pages 1–6. IEEE, 2018.
- [25] Youwei Zeng, Dan Wu, Ruiyang Gao, Tao Gu, and Daqing Zhang. Full-breathe: Full human respiration detection exploiting complementarity of csi phase and amplitude of wifi signals. *Proceedings of the ACM on Interactive, Mobile, Wearable and Ubiquitous Technologies*, 2(3):1–19, 2018.
- [26] Yanni Yang, Jiannong Cao, Xuefeng Liu, and Kai Xing. Multi-person sleeping respiration monitoring with cots wifi devices. In *2018 IEEE 15th International Conference on Mobile Ad Hoc and Sensor Systems (MASS)*, pages 37–45. IEEE, 2018.
- [27] Youwei Zeng, Dan Wu, Jie Xiong, Jinyi Liu, Zhaopeng Liu, and Daqing Zhang. Multisense: Enabling multi-person respiration sensing with commodity wifi. *Proceedings of the ACM on Interactive, Mobile, Wearable and Ubiquitous Technologies*, 4(3):1–29, 2020.
- [28] Gerrit Maus and Dieter Brückmann. Joint angle and respiration estimation for passive and device-free respiration monitoring. In *ICASSP 2023-2023 IEEE International Conference on Acoustics, Speech and Signal Processing (ICASSP)*, pages 1–5. IEEE, 2023.
- [29] Yi Tian Xu, Xi Chen, Xue Liu, David Meger, and Gregory Dudek. Pressense: Passive respiration sensing via ambient wifi signals in noisy environments. In *2020 IEEE/RSJ International Conference on Intelligent Robots and Systems (IROS)*, pages 4032–4039. IEEE, 2020.
- [30] Wei-Hsiang Wang, Beibei Wang, Xiaolu Zeng, and KJ Ray Liu. Wiresp: A robust wifi-based respiration monitoring via spectrum enhancement. *IEEE Sensors Journal*, 2024.
- [31] Jiaxing Hu, Jianfei Yang, Jenn-Bing Ong, Dazhuo Wang, and Lihua Xie. Resfi: Wifi-enabled device-free respiration detection based on deep learning. In *2022 IEEE 17th International Conference on Control & Automation (ICCA)*, pages 510–515. IEEE, 2022.
- [32] Dou Fan, Xiaodong Yang, Nan Zhao, Lei Guan, Malik Muhammad Arslan, Muneeb Ullah, Muhammad Ali Imran, and Qammer H Abbasi. A contactless breathing pattern recognition system using deep learning and wifi signal. *IEEE Internet of Things Journal*, 2024.
- [33] Shengjie Li, Zhaopeng Liu, Yue Zhang, Qin Lv, Xiaopeng Niu, Leye Wang, and Daqing Zhang. Wiborder: Precise wi-fi based boundary sensing via through-wall discrimination. *Proceedings of the ACM on Interactive, Mobile, Wearable and Ubiquitous Technologies*, 4(3):1–30, 2020.
- [34] Maciej Jan Niedźwiecki, Marcin Ciolek, Artur Gańcza, and Piotr Kaczmarek. Application of regularized savitzky-golay filters to identification of time-varying systems. *Automatica*, 133:109865, 2021.
- [35] Yangchang Xu and Ningning Xia. On the eigenvectors of large-dimensional sample spatial sign covariance matrices. *Journal of Multivariate Analysis*, 193:105119, 2023.
- [36] NTT Docomo et al. 5g channel model for bands up to 100 ghz. Technical report, Technical report, 2016.
- [37] Fusang Zhang, Zhi Wang, Beihong Jin, Jie Xiong, and Daqing Zhang. Your smart speaker can “hear” your heartbeat! *Proceedings of the ACM on Interactive, Mobile, Wearable and Ubiquitous Technologies*, 4(4):1–24, 2020.
- [38] Richard Rudd, Ken Craig, Martin Ganley, and Richard Hartless. Building materials and propagation. *Final Report, Ofcom*, 2604, 2014.



search interests include wireless sensing and mobile computing.

**Linqing Gui** received the Ph.D. degree in information science from INSA-Toulouse, Toulouse, France, in 2013. He is currently a Professor and a Ph.D. Supervisor with the School of Computers, Nanjing University of Posts and Telecommunications, Nanjing, China. His research papers have been published in premium international journals and conferences, including IEEE Transactions on Mobile Computing, IEEE Transactions on Dependable and Secure Computing, IEEE Transactions on Vehicular Technology, ACM UbiComp and ACM MobiHoc. His main re-



IEEE Internet Computing and IEEE Computer. He has received the ACM Distinguished Scientist award and Distinguished Speaker Award and the IBM Faculty Award. He is an elected member of Academia Europaea, where he's was Informatics Section chairman from 2015 to 2022. He is an IEEE Fellow and AAIA Fellow where he is the current President.

**Shahram Dustdar** (Fellow, IEEE) is a full professor of computer science and heads TU Wien's Distributed Systems Group. He is also ICREA Research Professor, UPF, Barcelona, Spain. His research interests include distributed systems, Edge Intelligence, complex and autonomic software systems. He's the editor in chief of Computing; associate editor of ACM Transactions on the Web, ACM Transactions on Internet Technology, IEEE Transactions on Cloud Computing, and IEEE Transactions on Services Computing. He's also on the editorial boards of



**Siyi Zheng** received the B.S. degree from the College of Computer and Information Engineering, Nanjing University of Technology, Nanjing, China, in 2022. He is currently pursuing the M.E. degree in the School of Computers, Nanjing University of Posts and Telecommunications, Nanjing, China. His research interests include wireless sensing and mobile computing.

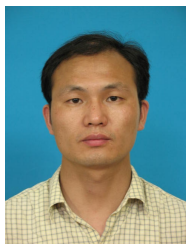


on Mobile Computing, ACM MobiCom, ACM UbiComp, ACM Sensys and ACM MobiHoc. His research interests include the Internet of Things and mobile computing. He is a member of the IEEE Computer Society and the Association for Computing Machinery.

**Fu Xiao** (Senior Member, IEEE) received the Ph.D. degree in computer science and technology from Nanjing University of Science and Technology, Nanjing, China, in 2007. He is currently a Professor and a Ph.D. Supervisor with the School of Computer Science, Nanjing University of Posts and Telecommunications, Nanjing. His research papers have been published in many prestigious conferences and journals, such as IEEE INFOCOM, IEEE/ACM Transactions on Networking, IEEE Journal on Selected Areas in Communications, IEEE Transactions



**Zhengxin Guo** received the Ph.D. degree in information network from the School of Internet of Things, Nanjing University of Posts and Telecommunications, Nanjing, China, in 2022. He is currently a lecturer with the School of Computer, Nanjing University of Posts and Telecommunications, Nanjing, China. His research interests include wireless sensing and mobile computing.



**Zhetao Li** received the B. Eng. from Xiangtan University in 2002, the M. Eng. degree from Beihang University in 2005, and the Ph.D. degree in Computer Application Technology from Hunan University in 2010. He is currently a professor with the College of Information Science and Technology, Jinan University, China. He was a visiting researcher at Ajou University from May to Aug 2012. His research interests include Wireless network, Internet of Things, Compressed sensing and big data.



**Ming Gao** received the Ph.D. degree in computer science and technology from Zhejiang University, in 2024. He is currently a Professor with the School of Computer Science, Nanjing University of Posts and Telecommunications, Nanjing. His research interests include IoT security, mobile computing and privacy protection. He is a recipient of the Best Paper Award Nomination from SenSys'21 and SenSys'24 and ACM SIGMOBILE Research Highlight in 2022.